

DOE/BC/15211-1
(OSTI ID: 13827)

IDENTIFICATION OF THE PERMEABILITY FIELD OF A POROUS
MEDIUM FROM THE INJECTION OF A PASSIVE TRACER

Topical Report
September 1999

By
Lang Zhan
Yanis C. Yortsos

Date Published: October 1999

Work Performed Under Contract No. DE-AC26-99BC15211

University of Southern California
Los Angeles, California



National Petroleum Technology Office
U. S. DEPARTMENT OF ENERGY
Tulsa, Oklahoma

DISCLAIMER

This report was prepared as an account of work sponsored by an agency of the United States Government. Neither the United States Government nor any agency thereof, nor any of their employees, makes any warranty, expressed or implied, or assumes any legal liability or responsibility for the accuracy, completeness, or usefulness of any information, apparatus, product, or process disclosed, or represents that its use would not infringe privately owned rights. Reference herein to any specific commercial product, process, or service by trade name, trademark, manufacturer, or otherwise does not necessarily constitute or imply its endorsement, recommendation, or favoring by the United States Government or any agency thereof. The views and opinions of authors expressed herein do not necessarily state or reflect those of the United States Government.

This report has been reproduced directly from the best available copy.

DOE/BC/15211-1
Distribution Category UC-122

Identification of the Permeability Field of a Porous Medium from the
Injection of a Passive Tracer

By
Lang Zhan
Yanis C. Yortsos

October 1999

Work Performed Under Contract DE-AC26-99BC15211

Prepared for
U.S. Department of Energy
Assistant Secretary for Fossil Energy

Thomas B. Reid, Project Manager
National Petroleum Technology Office
P.O. Box 3628
Tulsa, OK 74101

Prepared by
Petroleum Engineering Program
Department of Chemical Engineering
University of Southern California
Los Angeles, CA 90089-1211

TABLE OF CONTENTS

Abstract	v
I. INTRODUCTION	1
II. DIRECT INVERSION ALGORITHM: ISOTROPIC MEDIA	3
A Steamfunction Approach for 2-D Geometries	6
III. APPLICATIONS USING SIMULATED DATA	7
IV. A HYBRID ALGORITHM	11
V. DIRECT INVERSION ALGORITHM: ANISOTROPIC MEDIA	14
VI. CONCLUDING REMARKS	16
ACKNOWLEDGEMENTS	18
APPENDIX: Arrival Times for Circular Permeability Heterogeneity	18
REFERENCES	21
FIGURES	23-36

Abstract

We propose a method for the direct inversion of the permeability field of a porous medium from the analysis of the displacement of a passive tracer. By monitoring the displacement front at successive time intervals (for example, using a tomographic method), the permeability can be directly obtained from the solution of a non-linear boundary-value problem. Well-posedness requires knowledge of the pressure profile or the permeability at the boundaries of the system. The method is tested using synthetic data in 2-D (and some 3-D) geometries for a variety of heterogeneous fields and found to work well when the permeability contrast is not too large. However, it is sensitive to sharp variations in permeability. In the latter case, a modified approach based on the successive injection in both directions and the use of an optimization technique leads to improved estimates. An important feature of the direct method is that it also applies to anisotropic porous media. When the principal axes of anisotropy are known, a suitable procedure is proposed and demonstrated using synthetic data.

I. INTRODUCTION

Permeability heterogeneity is a most important feature of natural porous media, as it affects significantly flow and fluid displacement properties. These dictate flow paths, and the migration and dispersion of in-situ or injected fluids in porous media, with applications ranging from the recovery of in-situ fluids to the fate of environmental contaminants in the subsurface [1]. Heterogeneity is manifested at various scales, from the laboratory (core) to the megascopic (field) scale. Its ubiquitous and multi-scale nature has attracted the interest of many investigators, and a variety of studies have been devoted to its characterization and identification [2].

The classical approach for identifying permeability heterogeneity is based on the inversion of pressure data, under single-phase flow conditions [3]. Given that the transient flow of slightly compressible fluids obeys the diffusion equation, a variety of field tests (well tests) have been devised to infer permeability features by matching pressure data at well locations to the solution of the diffusion equation. While significant advances can be made with this approach, the sparsity of data restricts the detail as well as the uniqueness of the characterization. Pressure transient methods have also been applied to characterize the heterogeneity of laboratory cores, using mini-permeameters [4]. These devices conduct mini-well tests on the surface of a laboratory core (by injecting a small pulse of air and monitoring the resulting pressure transient) and essentially provide a map of the permeability heterogeneity at the external surface of the sample.

An alternative approach to permeability identification is based on the analysis of the arrival times during the injection of passive tracers (namely of tracers which do not affect the fluid viscosity and density). Various efforts have been made at the field scale to relate the arrival times to the permeability, and to match assumed permeability fields to such data [5]. These techniques are usually indirect, based on optimizing arbitrary (or constrained) initial guesses to match data at various, usually sparse, locations. As a result, they suffer from non-uniqueness. Nonetheless, useful information can be extracted, which can be used to constrain images of the subsurface permeability field.

When knowledge of the displacement front at successive time intervals is available, for example through visual or tomographic techniques, arrival time methods should in principle

be able to provide direct maps of the permeability heterogeneity. Brock and Orr [6] reported one such attempt, using qualitative arguments, based on the visualization of displacements in a 2-D heterogeneous bead pack. Withjack et al. [7] considered the application of X-ray Computerized Tomography (CT). They proposed a model to infer the permeability heterogeneity from the analysis of CT-derived concentration contours. Their model is based on a number of simplifying assumptions, the main of which is that each streamtube has constant (but unknown) permeability and porosity, and is, thus, tantamount to an assumption of a layered structure. Although restrictive, the work of Withjack et al. [7] was the first to point out the potential of CT in identifying the permeability heterogeneity of porous media. CT techniques are now routinely applied to monitor displacement fronts in porous media at the laboratory scale. Advances in field scale tomography, for example by seismic methods or cross-hole tomography, are also likely to lead to analogous results at the field scale [8]. Yet, well-defined methods to invert such information to determine the permeability heterogeneity are currently lacking.

In this paper, we propose a new method which focuses on this question, namely on how to invert data on arrival times at various (and numerous) points in the porous medium to map the permeability field. The method, elements of which were briefly described in [9], is based on a direct inversion of the data, as will be described below, rather than on the optimization of initial random (or partly constrained) guesses of the permeability field, to match the available data, as typically done in the analogous problem of pressure transients. The direct inversion is based on two conditions, that Darcy's law for single-phase flow in porous media is valid, and that the dispersion of the concentration of the injected tracer is negligible. While the former is a well-accepted premise, the latter depends on injection and field conditions, and may not necessarily apply in all cases. Based on these conditions, we formulate a non-linear boundary value problem, the coefficients of which depend on the experimental arrival time data. Because of the hyperbolic nature of the problem, uniqueness requires that either the permeability or the pressure at the bounding surface of the porous medium be available. This information is then combined to obtain a solution of the boundary-value problem from which the permeability field can be directly calculated. An important feature of the method is that it can be applied to determine the heterogeneity of anisotropic media, where the

permeability field is a tensor, as is often the case in many natural porous media. For this, displacements in two (for 2-D) or three (for 3-D) different directions must be conducted, as will be described below.

In our approach, the experimental information on arrival times enters in the form of spatial derivatives. As a result, the solution method is sensitive to errors in the estimation of these derivatives, which are expected to increase when the variations in the permeability are sharp and large. The errors are magnified around certain limiting streamlines, the width of which increases in the downstream direction, and may lead to poor estimates of the permeability in some regions. To circumvent this problem, we have modified the inversion method in such cases, by considering a *forth-and-back* hybrid approach, in which arrival times are recorded a second time by repeating the tracer displacement in the reverse direction. This approach is then combined with an optimization technique to improve the resulting estimates.

The paper is organized as follows: In section II we describe the inversion method for isotropic media. Section III shows numerical examples which test the applicability of the method for various forms of permeability heterogeneity and its sensitivity to permeability variation and spatial correlation. Section IV describes the hybrid approach for inverting permeability fields with sharp and large contrasts. The extension of the method to anisotropic media of known and fixed principal axes is presented in section V. We close with a related discussion and concluding remarks.

II. DIRECT INVERSION ALGORITHM: ISOTROPIC MEDIA

We consider the injection in a heterogeneous and isotropic porous medium of a passive tracer. In the absence of dispersion, the concentration $C(\mathbf{x}, t)$ satisfies the equation

$$\phi(\mathbf{x}) \frac{\partial C}{\partial t} + \mathbf{v} \cdot \nabla C = 0 \quad (1)$$

where $\phi(\mathbf{x})$ is the porosity of the medium and \mathbf{v} is the superficial fluid velocity. Under slow, viscous flow conditions, the latter satisfies Darcy's law

$$\mathbf{v} = -\mathbf{K} \cdot \nabla \Phi \quad (2)$$

where $\mathbf{K}(\mathbf{x})$ is the symmetric permeability tensor and Φ is a flow potential, $\nabla\Phi = \frac{1}{\mu}(\nabla p - \rho\mathbf{g})$, where μ is viscosity, here taken as a constant, p is pressure, ρ is density, also assumed constant, and \mathbf{g} is the acceleration of gravity. In this section, permeability is assumed to be a scalar, $\mathbf{K}(\mathbf{x}) = k(\mathbf{x})\mathbf{I}$, where \mathbf{I} is the identity tensor. The anisotropic case is discussed in Section V. Assuming incompressible fluids, the continuity equation reads

$$\nabla \cdot \mathbf{v} = 0 \quad (3)$$

In the absence of dispersion, we define the front location by the equation

$$\mathcal{F}(\mathbf{x}, t) \equiv t - f(\mathbf{x}) = 0 \quad (4)$$

where, assuming constant or monotonic injection rates, the function $f(\mathbf{x})$ is single-valued, thus a single arrival time is associated with a given point \mathbf{x} . Then, the concentration is given by

$$C(\mathbf{x}, t) = C_i(t)H(t - f(\mathbf{x})) \quad (5)$$

where $C_i(t)$ is the injection concentration, and H is the Heaviside step function.

The direct algorithm is based on the following two steps: First, we equate the two expressions for the normal velocity at the front, given by the kinematics and by Darcy's law, respectively. Noting that the normal at the front is given by

$$\mathbf{n} = \frac{\nabla\mathcal{F}}{|\nabla\mathcal{F}|} = -\frac{\nabla f}{|\nabla f|} \quad (6)$$

we use (5) and (6) in (1) to obtain a kinematic expression for the normal velocity there, namely

$$v_n = -\frac{\phi(\mathbf{x})}{|\nabla f|} \quad (7)$$

Darcy's law (equations (2) and (6)) gives another expression for the same quantity

$$v_n = \frac{k(\mathbf{x})\nabla\Phi \cdot \nabla f}{|\nabla f|} \quad (8)$$

Thus, (7) and (8) lead to the following result for the permeability

$$k(\mathbf{x}) = -\frac{\phi(\mathbf{x})}{\nabla\Phi \cdot \nabla f} \quad (9)$$

which, in principle, can be evaluated in terms of Φ and f . The second step consists of substituting the above expression in Darcy's law and making use of the continuity equation (3) to obtain a non-linear equation for Φ ,

$$\nabla \cdot \left[\frac{\phi(\mathbf{x})\nabla\Phi}{\nabla\Phi \cdot \nabla f} \right] = 0 \quad (10)$$

Equations (9) and (10) constitute the keys of the direct inversion method. Equation (10) is a partial differential equation which determines Φ given appropriate boundary conditions and information on the porosity, $\phi(\mathbf{x})$, and the arrival time function, $f(\mathbf{x})$. From its solution, the permeability field can be directly calculated using (9).

The following remarks are in order:

1. For the solution of (10), the porosity must be a known function of the spatial coordinates. For applications using CT, this can be readily available.

2. Although at first glance equation (10) appears to be an elliptic (Laplace type) equation, it is in fact a system of first-order hyperbolic equations. This can be readily shown, e.g. in 2-D, by defining

$$u \equiv \frac{\frac{\partial\Phi}{\partial y}}{\frac{\partial\Phi}{\partial x}} \quad (11)$$

in which case (10) becomes

$$\frac{\partial}{\partial x} \left[\frac{\phi(\mathbf{x})}{f_x + u f_y} \right] + \frac{\partial}{\partial y} \left[\frac{\phi(\mathbf{x})u}{f_x + u f_y} \right] = 0 \quad (12)$$

where subscripts indicate partial derivatives (and similarly for 3-D). These two equations (11) and (12) form a pair of first-order hyperbolic equations. For their solution, and thus for the solution of (10), information on the potential Φ at the (no-flow) boundaries is necessary. Equivalently, this information can be furnished from a knowledge of the permeability at the boundaries (which, for instance, can be obtained by a mini-permeameter, as previously noted). At no-flow boundaries (where in the normal direction $\frac{\partial\Phi}{\partial n} = 0$), equation (9) becomes

a partial differential equation for the variation of Φ along the two tangential directions (for the 3-D case), which can be integrated, given k and f at the boundary, to yield the required profile. We must point out, however, that in all applications to be shown below, we solved (10) assuming known pressure profiles at all boundaries. In this way, the numerical method utilizes information from all boundaries, essentially solving an elliptic-like, rather than a hyperbolic system.

3. A notable feature of (9) and (10) is that they depend on the gradient of the front arrival time rather than the arrival time itself. On the positive side, this reflects a desirable sensitivity of the method to heterogeneity. However, this dependence also introduces numerical instability which can lead to problems when the permeability contrast is sharp and large. A technique to circumvent these problems is described later in Section IV.

In summary, supplied with boundary conditions on the potential, equations (9) and (10) can be solved directly to yield the permeability field in a heterogeneous porous medium based on information on arrival times and the porosity heterogeneity. The resolution of the inverted permeability field depends, among others, on the resolution of the arrival time contours.

A Streamfunction Approach for 2-D Geometries

Before proceeding, it is worthwhile to note that in 2-D geometries, an alternative inversion method is possible, based on the use of the streamfunction Ψ , where $\frac{\partial \Psi}{\partial y} = v_x$ and $\frac{\partial \Psi}{\partial x} = -v_y$. Indeed, rearrangement of (7) leads to

$$\frac{\partial f}{\partial y} \frac{\partial \Psi}{\partial x} - \frac{\partial f}{\partial x} \frac{\partial \Psi}{\partial y} = -\phi(\mathbf{x}) \quad (13)$$

which is a first-order, hyperbolic differential equation for Ψ . The characteristics of the latter are curves of constant f , namely of constant arrival time, which are available experimentally. Therefore, the streamfunction can be computed by integrating along these contours, for example

$$\Psi = \Psi_0 + \int_{y_0}^y \frac{\phi}{f_x} dy \quad (14)$$

where, in the case of a rectilinear sample with a no-flow boundary at $y_0 = 0$, we can take $\Psi_0 = 0$ without loss. To compute the potential we make use of the fact that in the isotropic case, equipotentials are orthogonal to the streamlines, hence

$$\frac{\partial \Psi}{\partial x} \frac{\partial \Phi}{\partial x} + \frac{\partial \Psi}{\partial y} \frac{\partial \Phi}{\partial y} = 0 \quad (15)$$

This hyperbolic equation can also be integrated subject to appropriate boundary conditions. Then, the permeability can be estimated from (9), or from the alternative expression $k = \frac{\partial \Psi}{\partial y} / \frac{\partial \Phi}{\partial x}$. Illustrative examples using this approach are discussed below.

III. APPLICATIONS USING SIMULATED DATA

The direct inversion method was subsequently tested based on simulated data. We used a high-resolution finite-difference simulator (the main features of which are described in [10]) or a streamline-based method to simulate tracer displacement and provide data on arrival times and the pressure profile at the boundaries. The displacement corresponds to constant-rate injection in the absence of gravity. The boundary value problem (10) was solved using a standard SOR finite-difference formalism, which was iterated until convergence. For example, for the 2-D geometry we used the five-point scheme

$$\begin{aligned} & \Theta_{i+1/2,j}^m \Phi_{i+1,j}^{m+1} + \Theta_{i-1/2,j}^m \Phi_{i-1,j}^{m+1} + \Theta_{i,j+1/2}^m \Phi_{i,j+1}^{m+1} + \Theta_{i,j-1/2}^m \Phi_{i,j-1}^{m+1} \\ & - (\Theta_{i+1/2,j}^m + \Theta_{i-1/2,j}^m + \Theta_{i,j+1/2}^m + \Theta_{i,j-1/2}^m) \Phi_{i,j}^{m+1} = 0 \end{aligned} \quad (16)$$

where $\Theta_{i,j}^m$ is the conductivity coefficient at block (i, j) at iteration level m . All other coefficients were evaluated using the harmonic average between $\Theta_{i,j}^m$ and its nearest neighbor. An interpolation routine was used to interpolate the arrival times, when necessary. The spatial derivatives of f were calculated using three-point differences. Equation (16) was solved using the prescribed pressure profiles on both no-flow boundaries. Parenthetically, we note that the forward problem belongs to the general class of problems recently discussed by Sethian [11], and can benefit from the application of a Fast Marching Technique. Such was not implemented here, however.

Figs. 1-3 show results of the application of the inversion method in three 2-D heterogeneity fields of a moderate permeability contrast, corresponding to a layered medium, a medium with a smoothly varying heterogeneity and a permeability distribution following fBm (fractional Brownian motion) statistics. Each figure shows true and directly inverted permeability fields, along with true and directly inverted and potential profiles. In all these examples, the direct inversion is found to give very good results.

Fig. 1 shows that the method handles well permeability contrasts transversely to the direction of displacement, with some expected dispersion around the discontinuity. Potential profiles are also reproduced well, again with some differences noted around the discontinuity. We must emphasize that in this example, the success of the method rests on the availability of the potential profile at the boundary, which removes the non-uniqueness of the problem. (Indeed for a 1-D displacement with piecewise constant permeability at constant injection rate, equation (10) becomes indeterminate). Likewise, good results were found when the permeability contrast was in the direction parallel to the displacement. The ability of the method to invert the permeability field in the presence of an arbitrary closed region of sharp permeability contrast is discussed in a later section.

The permeability field of Fig. 2 is smoothly varying and contains two peaks and one valley, with a permeability contrast of about 2. It was generated in a 64×64 grid using Franke's test function from MATLAB [12]. This function often serves as a test for the interpolation of scattered data. It is noted that the arrival times are much more sensitive to the heterogeneity, than the pressure profiles, which are essentially parallel to the transverse direction. This feature was noted in other cases as well, where the permeability variation is relatively smooth. Fig. 2 shows that the comparison between actual and inverted fields (in permeability and potential profiles) is very good. This example is characteristic of the success of the method in smoothly varying permeability fields.

A more stringent test is shown in Fig. 3 with a similar permeability contrast. The permeability field is of the fBm type with a Hurst exponent $H = 0.8$, and it is a typical example of a self-affine field, containing large-scale correlations [13]. We remark that fBm statistics with a Hurst exponent larger than 0.5 are often assumed to describe the heterogeneity in the horizontal permeability of natural rocks [14]. Fig. 3 shows that the match

between actual and inverted data is also quite good. Potential profiles are closely matched. The inverted permeability reproduces well the main features of this field, namely the regions where the permeability is respectively high, medium or low. However, discrepancies can also be detected in the point-by-point variation of the permeability, where the inverted field is somewhat smoother than the actual. The ability to capture long-wavelength, as opposed to high-frequency, variations is typical of the technique and was noted in other examples, as well. Fig. 4 shows a statistical analysis of the actual and inverted permeabilities. Histograms and the correlation structure (the semi-variograms) match quite well, and the scatter plot is satisfactory. The dispersion around the 45° line indicates a small degree of point-by-point mismatch, as also evidenced in Fig. 3.

The direct inversion technique is equally well applied to 3-D geometries. Before we proceed, however, it is instructive to compare inversion results using the 2-D streamfunction method. Figs. 5 and 6 show the resulting permeability estimates, along with the associated streamfunctions, corresponding to Figs. 2 and 3, respectively. Although the streamlines are well reproduced, it is evident that the inverted permeability fields, although maintaining the large correlation features, miss significant details. There are also notable defects extending along slice-shaped regions, which arise from the integration along the arrival time contours. A statistical analysis, not shown here for lack of space, shows that the inverted permeability reproduces reasonably well the semi-variograms. However, the histograms, and to a greater degree, the scatter plot, have large errors in several places. The streamfunction method is prone to relatively large numerical errors, because it involves a threefold interpolation for spatial derivative estimation and the integration of hyperbolic equations (for determining the streamfunction). These weaknesses make the method unfavorable compared to the direct solution of (9) and (10) (as seen in the comparison of Figs. 2 to 5 and 3 to 6). Advantages of the method, on the other hand, are that the permeability is inverted fast, compared to the previous, while one also readily obtains the streamfunction profile, which may be useful in other applications.

To demonstrate the applicability of the direct inversion method to three dimensions, we considered the 3-D permeability field shown in Fig. 7a, consisting of a log-normal distribution generated by Sequential Gaussian Simulation, with a natural logarithmic mean of 2.0, a

standard deviation of 0.2 and a dimensionless correlation length (with respect to the sample size) of 0.5. The permeability variation is somewhat larger than before. Characteristic arrival time contours from the simulation of the forward problem in a $16 \times 16 \times 16$ lattice are shown in Fig. 7b. The direct inversion algorithm was applied by using a 3-D version of (16) along with boundary conditions supplied from the forward problem. The results of the permeability inversion in Fig. 8 appear to be in relatively good agreement with the actual (Fig. 7a). A more quantitative comparison is shown in the statistics of Fig. 9, which is calculated by GSLIB [15]. In general, the comparison is good. The inverted field shows a smaller range of variation than the actual, as reflected in both the semi-variogram and the histogram. Notably, the spatial correlation structure of the former is well captured in the inverted data. The scatter plot indicates somewhat larger dispersion, compared to the fBm field of Figs. 3-4, which is expected, given the larger permeability contrast in this example.

In the above examples, where the permeability contrast is not too large, or where the permeability has relatively large spatial correlations, the direct inversion method gives good results. When the contrast increases and variations in permeability are sharper, however, the method is subject to increased errors. These primarily arise from the approximation of the spatial gradients of the arrival time in regions where the latter varies sharply. For example, Fig. 10 shows arrival time contours, calculated analytically (see Appendix), for flow around an embedded sphere of lower permeability. Even though the permeability contrast is relatively modest (0.6:1), there exist two layers, extending downstream of the sphere, where the arrival times have sharp spatial variations. These layers are centered around the two limiting streamlines tangent to the sphere. In these regions, the evaluation of the coefficients of (10) is likely to introduce errors, and accordingly poor estimates for the permeability in some places. These limiting streamlines also exist in any other field containing regions of sharp permeability contrast. Because these zones extend downstream of the region of the sharp contrast, however, the associated errors in permeability estimates are different depending on the direction of displacement. We have conjectured, therefore, that the estimates of the direct method could be improved substantially, if we were to combine information from two different displacements, one in the forward and the other in the reverse direction.

IV. A HYBRID ALGORITHM

To circumvent the problems posed by high permeability contrasts we propose the following hybrid procedure:

1. Carry out a tracer displacement in the forward direction and directly invert to obtain one permeability estimate, $k_f(\mathbf{x})$.
2. Carry out a tracer displacement in the reverse direction and directly invert to obtain a second permeability estimate, $k_b(\mathbf{x})$.
3. Retain the estimates in places, where they differ in absolute value by no more than a prescribed value and discard in all others. Assign estimates in these regions by an interpolation algorithm (known in the geostatistics literature as kriging).
4. Use an optimization algorithm (to be briefly described below) to fine-tune the so obtained composite permeability estimates.

The optimization algorithm is based on standard gradient methods [16] and will not be discussed here in any detail. We briefly note that we use the objective function

$$\mathcal{J} = \frac{1}{2} \left\{ \sum_{i=1}^N W_{1i} [f_i(\mathbf{k}) - f_i^m]^2 + \sum_{i=1}^M W_{2i} [k_i - k_i^p]^2 + \sum_{i=1}^L W_{3i} [\Phi_{bi} - \Phi_{bi}^m]^2 \right\} \quad (17)$$

where, the first term in the RHS is the weighted sum of the squares of the differences between the front arrival times obtained from the simulator response, f_i , and the data, f_i^m , and the third is the analogous term for the differences between the potential at the no-flow boundaries obtained from the simulator, Φ_{bi} , and the data, Φ_{bi}^m . The second term represents the mismatch between the current permeability estimate and its prior. It is a regularization term, as required by Tikhonov's theory [17], and restricts the parameters being optimized to not deviate greatly from the prior information. Numerical experience has demonstrated the necessity of this term for stable and convergent solutions. Nonetheless, the accuracy of the initial guess plays a pivotal role in the convergence to the true solution. It is in this context, that the hybrid algorithm offers an important advantage. Here, the prior information is supplied using the direct inversion method, outlined in steps 1-3 above, which is generally close to the true permeability field. As a result, in many of the cases tried, the optimization method converges close to the true values. By contrast, in many related inverse problems, the

prior permeability is typically generated by a geostatistical algorithm constrained to (usually) sparse measurements, and its convergence to the true solution is generally uncertain (e.g. see [26]). At the same time, we must stress that we have also encountered many problems involving sharp permeability contrasts, which cannot be successfully handled even with the hybrid algorithm. Such an example will be shown below.

Applications of the hybrid algorithm using simulated data are illustrated in Figs. 11-14 for three different examples. The medium in Fig. 11 contains two blocks of low permeability with a 1:5 contrast. This particular configuration corresponds to the experimental Hele-Shaw cell used in [19], and was discretized by a 22×10 lattice. The top of Fig. 11 (panels a,b) shows the prior estimate fed to the optimization algorithm, following the steps 1-3. Due to the sharp permeability contrast between low and high permeable regions, the spatial derivatives of the arrival times have significant numerical errors in certain regions, and lead to a mismatch between true and inverted values in various places after steps 1 and 2. Through step 3 (where estimates were discarded when they differed by more than 30%), these errors have been minimized and the directly inverted field (Fig. 11, a,b) has the main trends of the true field, although it is obvious that the contrast is not as sharp as the actual, and is in need of fine-tuning. The results of the application of the optimization algorithm of step 4, using 40 iterations, and based on the initial guess after kriging (top of Fig. 11), is shown in the middle of Fig. 11 (panels c,d). The results are much improved and, with a few exceptions, they are very close to the actual. Although not shown, potential and arrival time profiles are also matched very well. By contrast, if a uniform initial guess, instead of the one after the direct method on the top of Fig. 11, was used in the optimization algorithm, the resulting estimate of the permeability field (after the same number of iterations) is poor in many places, as shown in the bottom of Fig. 11 (panels e,f). This, despite the fact that arrival times and potential profiles were found to match very well. We conclude that, at least for this example, the application of the hybrid method gives a substantial improvement.

Fig. 12 shows the application of the algorithm to a correlated log-normal distribution with a logarithmic mean of 2.0, a standard deviation of 0.5 and a dimensionless correlation length of 0.25. In this example, the block-to-block permeability variation is much larger than in the fBm field of Fig. 3 or the 3-D field of Fig. 7, the largest contrast being of an order of

magnitude. The application of the direct inversion method followed by kriging leads to the results shown in the middle of Fig. 12 (panels c,d). Although capturing the general features of the true field, the estimates are generally coarser and smoother than the actual values. Comparison of arrival time and potential profiles based on the inverted field (not shown for lack of space) indicates a mismatch with the actual in some places. To fine-tune the results and recover some of the high-frequency variations, we applied the optimization algorithm of step 4. Results after 40 iterations are shown on the right of Fig. 12 (panels e,f). Although the algorithm does not reproduce exactly the actual field, and some errors around large variations of permeability are detectable, it is obvious that a significant improvement has been achieved. Fig. 13 shows the corresponding statistical comparison. The mean and the variance from the hybrid algorithm agree very well with the actual. (By contrast, in results that are not shown, the variance from kriging is underestimated by about 20%, although the mean is the same.) The two histograms are roughly equal, while the semi-variograms have the same correlation structure. The scatter plot shows that good agreement exists over a good range of lower permeabilities, although an increasing scatter can be seen at larger permeabilities. In this example, these are typically associated with large contrasts. We need to reiterate that the success of the hybrid algorithm depends to a large extent on the accuracy of the initial guess, which is here provided by the direct method and positions the optimization scheme close to the true solution. By contrast, the estimates resulting from the application of the same optimization algorithm after bypassing steps 1-3 and utilizing a uniform initial guess were quite poor, even though arrival times and potential matched nearly perfectly with the true values.

At the same time, we must point out that we have also encountered several cases where the hybrid algorithm was not as successful as desired. Fig. 14 (panels a,b) is an example of a “checkerboard”-pattern heterogeneous field, with a permeability contrast of 1:4. A pattern similar to this was used in some tracer displacement experiments [20]. The results of the algorithm at the end of the kriging step are shown in the middle of Fig. 14 (panels c,d). The mismatch with the true data is quite apparent. The 2-D projection in the middle of Fig. 14 reproduces roughly the places of maximum permeability variation, but the picture is clearly “out of focus”. The results of the application of the optimization method are shown

in the right of Fig. 14 (panels e,f). We note a clear improvement, compared to the previous step, and a better focused image. Yet, there is also clear evidence of mismatches in various places, including the smoothing of the sharp contrast around the edges of discontinuity and of other defects, which altogether preclude an exact matching. Thus, although overall the hybrid algorithm appears to be a promising alternative in cases involving large contrasts, we caution that this is not uniformly true and that many counter-examples can readily be constructed where the algorithm will not be as successful.

V. DIRECT INVERSION ALGORITHM: ANISOTROPIC MEDIA

On the other hand, a strong attribute of the technique proposed is that it can be readily applied to anisotropic porous media. In this section, we consider for simplicity 2-D geometries, where the principal directions of the permeability tensor are constant and coincide with the rectangular coordinates x and y , namely we will assume that

$$\mathbf{K} = \begin{vmatrix} k_x(\mathbf{x}) & 0 \\ 0 & k_y(\mathbf{x}) \end{vmatrix} \quad (18)$$

An extension to the more general case is under consideration and will be presented elsewhere. Under these conditions, the equations analogous to (9) and (10) read as follows

$$(\mathbf{K} \cdot \nabla \Phi) \cdot \nabla f = -\phi(\mathbf{x}) \quad (19)$$

and

$$\nabla(\cdot \mathbf{K} \cdot \nabla \Phi) = 0 \quad (20)$$

Using scalar notation, and substituting from (18), we further have

$$k_x \frac{\partial \Phi}{\partial x} \frac{\partial f}{\partial x} + k_y \frac{\partial \Phi}{\partial y} \frac{\partial f}{\partial y} = -\phi \quad (21)$$

and

$$\frac{\partial}{\partial x} \left[k_x \frac{\partial \Phi}{\partial x} \right] + \frac{\partial}{\partial y} \left[k_y \frac{\partial \Phi}{\partial y} \right] = 0 \quad (22)$$

Equations (21) and (22) constitute a pair of two equations in three unknowns (k_x , k_y and Φ) and require additional information for their solution. One possible approach to furnish this information is by conducting two tracer displacements, one in the x -direction with no-flow boundaries perpendicular to the y -axis, and another in the y -direction with no-flow boundaries perpendicular to the x -axis. If we denote the arrival time functions and the potentials of the two displacements by f_I and f_{II} , and Φ_I and Φ_{II} , respectively, Eq. (21) becomes

$$k_x \frac{\partial \Phi_I}{\partial x} \frac{\partial f_I}{\partial x} + k_y \frac{\partial \Phi_I}{\partial y} \frac{\partial f_I}{\partial y} = -\phi, \quad (23)$$

$$k_x \frac{\partial \Phi_{II}}{\partial x} \frac{\partial f_{II}}{\partial x} + k_y \frac{\partial \Phi_{II}}{\partial y} \frac{\partial f_{II}}{\partial y} = -\phi \quad (24)$$

for the respective displacements. Thus, the permeability components can be determined

$$k_x = -\frac{\phi}{A} \left[\frac{\partial \Phi_{II}}{\partial y} \frac{\partial f_{II}}{\partial y} - \frac{\partial \Phi_I}{\partial y} \frac{\partial f_I}{\partial y} \right] \quad (25)$$

and

$$k_y = -\frac{\phi}{A} \left[\frac{\partial \Phi_I}{\partial x} \frac{\partial f_I}{\partial x} - \frac{\partial \Phi_{II}}{\partial x} \frac{\partial f_{II}}{\partial x} \right] \quad (26)$$

where

$$A = \frac{\partial \Phi_I}{\partial x} \frac{\partial f_I}{\partial x} \frac{\partial \Phi_{II}}{\partial y} \frac{\partial f_{II}}{\partial y} - \frac{\partial \Phi_{II}}{\partial x} \frac{\partial f_{II}}{\partial x} \frac{\partial \Phi_I}{\partial y} \frac{\partial f_I}{\partial y} \quad (27)$$

in terms of the given data f_I and f_{II} , and the calculated potentials Φ_I and Φ_{II} . The latter can be obtained by solving equation (22), with k_x and k_y given by (25)-(27), and with the appropriate boundary conditions corresponding to the two different displacements. To solve the resulting coupled system, we implemented the following iterative algorithm:

1. Based on the ν -level estimates for the potentials Φ_I^ν and Φ_{II}^ν , use Eqs. (25) and (26) to estimate the ν -level iterates k_x^ν and k_y^ν . At the initial iteration ($\nu = 0$), an initial guess, typically in the form of a linear variation, is supplied for the potentials.
2. Based on explicit (ν -level) estimates for k_x^ν and k_y^ν , integrate (22) twice, using SOR finite differences to calculate the potentials at the next iteration level, $\Phi_I^{\nu+1}$ and $\Phi_{II}^{\nu+1}$.

This algorithm was found to work well for the various cases tested so far.

The method was subsequently applied to the anisotropic permeability field shown in the left of Figs. 15-16 (panels a,b). Its statistics are similar to Fig. 7, and involve a log-normal spatially correlated distribution with the same mean and standard deviation. By simulating tracer displacements in the two directions, x and y , respectively, we obtained the respective arrival time functions and potentials at the no-flow boundaries, which were used for the inversion according to the above scheme. The directly inverted fields are shown in the right of the two Figs. 15-16 (panels c,d). Considering the coupled nature of the problem, the reconstruction of the two permeability components is generally good. The method reproduces relatively well the regions of high and low permeability. Compared to the isotropic case under the same permeability contrast, however, the reconstruction is not as sharp, and the projections of the inverted images appear slightly “out of focus” in certain places. This mismatch reflects an underlying slight mismatch in the arrival times and the potential profiles, which is not shown here. Further work is under way to improve the algorithm and fine-tune the direct inversion method, including the implementation of a hybrid algorithm as in the isotropic case.

VI. CONCLUDING REMARKS

In this paper we presented a method for the direct inversion of the permeability of porous media, based on arrival time contours and information on the pressure profiles at the boundaries. The former can be obtained in real systems using techniques of visualization, computerized tomography or cross-hole tomography. The method utilizes Darcy’s law for flow in porous media in combination with the kinematics of flow, as expressed in the arrival times, to derive a boundary-value problem, the solution of which leads to a direct reconstruction of the permeability field. An important feature of the technique is that the information from the pressure at the boundaries is used to formulate and solve an elliptic-like formulation, rather than the two hyperbolic equations, which formally describe the problem. The algorithm developed is a rigorous tool for the analysis of arrival time contours.

Using simulated data, the method was found to work well for cases, where the permeability contrast is not very large, and the field is spatially correlated. In general, the technique

captures well variations corresponding to larger wavelengths, but not as well the fine-scale details. For sharper contrasts, a hybrid version of the algorithm was developed, in which the direct method is used to generate the initial guess in an optimization algorithm. The hybrid version minimizes the sensitivity of the method to errors in spatial derivatives, which are augmented in the presence of sharp contrasts. Examples in two and three dimensions using simulated data demonstrated that the hybrid algorithm works well and that it is superior to the more conventional case, where the initial input is a uniform distribution. However, other examples can also be constructed, involving sharp contrasts, where the inversion technique is not as satisfactory and requires further improvement. A second advantage of the direct inversion technique is its potential to invert the permeability tensor in anisotropic porous media. Preliminary results for the case where the principal axes of anisotropy are fixed and known were presented and found to be promising. Further work is currently under way to fine-tune the method and to also extend it to the more general case, where the permeability tensor is full.

The applicability of the technique to real systems relies on several conditions: the availability of pressure profiles at the system boundaries, the absence, or the minimization, of dispersion during the tracer displacement and the availability of an adequate resolution in arrival time contours. The first requirement appears to be the most difficult to meet, in practice, in view of the demand for adequate spatial resolution, which presently available tools may not possess, and the need to enforce Darcy's law near no-flow boundaries. Alternatively, this profile can be obtained by locally probing the surfaces with a mini-permeameter to construct a surface permeability map, from which the pressure profile can be computed. A certain amount of dispersion is also unavoidable, in real porous media, where the dispersion coefficient is proportional to the velocity, thus leading to a constant Peclet number and a finite amount of dispersion. However, for relatively small dispersivities, dispersion effects could be minimized. Sufficient spatial resolution on arrival times would allow to capture fine-scale variations, at the expense of increased computational time in the optimization routine of the hybrid algorithm, and possible instabilities as the degree of resolution increases. However, it must also be remarked that in our experience, so far, a coarse-grid reconstruction can adequately capture the large-scale features of the permeability field, both in the isotropic

and the anisotropic cases. The process of validation of the method with actual experimental data is currently under way.

ACKNOWLEDGMENTS

This research was partly supported by DOE Contracts DE-FG22-96BC1994/SUB and DE-AC2699BC15211, the contributions of which are gratefully acknowledged. We would like to thank Roland Lenormand and Dominique Salin for useful comments and discussions. The contribution of the NATO travel grant CRG 973049 is also gratefully acknowledged.

APPENDIX:

Arrival Times For Circular Permeability Heterogeneity

In this appendix, we provide analytical solutions for a simple 2-D problem involving tracer displacement in an infinite domain of constant permeability 1, in which a circular inclusion of radius $r = 1$ and permeability κ is embedded. Thus, the permeability is the step function

$$k = (1 - \kappa)H(r - 1) + \kappa \tag{A-1}$$

Subtracting the homogeneous solution ($-x$) from the potential, we next consider the solution of

$$\nabla \cdot [k\nabla(x + \psi)] = 0 \tag{A-2}$$

where $\psi = -\Phi + x$. Thus,

$$\nabla \cdot (k\nabla\psi) = -(\kappa + 1)\delta(r - 1)\frac{x}{r} \tag{A-3}$$

where δ denotes the Dirac delta function. To solve (A-3) we use polar coordinates (r, θ) and the following interface conditions at the permeability discontinuity

$$\psi|_{r=1+} = \psi|_{r=1-} \tag{A-4}$$

and

$$\kappa \frac{\partial \psi}{\partial r} \Big|_{1-} - \frac{\partial \psi}{\partial r} \Big|_{1+} = (1 - \kappa) \cos \theta. \quad (\text{A-5})$$

The solution is obtained in straightforward fashion

$$\psi = \left(\frac{1 - \kappa}{1 + \kappa} \right) r \cos \theta \quad ; \quad r \leq 1 \quad (\text{A-6})$$

$$\psi = \left(\frac{1 - \kappa}{1 + \kappa} \right) \frac{1}{r} \cos \theta \quad ; \quad r > 1 \quad (\text{A-7})$$

from which the velocity components can be calculated. We find,

$$v_x = \frac{2\kappa}{1 + \kappa} \quad ; \quad r \leq 1$$

$$v_x = 1 + \left(\frac{1 - \kappa}{1 + \kappa} \right) \frac{y^2 - x^2}{(x^2 + y^2)^2} \quad ; \quad r > 1$$

and

$$v_y = 0 \quad ; \quad r \leq 1$$

$$v_y = - \left(\frac{\kappa(1 - \kappa)}{1 + \kappa} \right) \frac{2xy}{(x^2 + y^2)^2} \quad ; \quad r > 1$$

Finally, the streamlines are the solution of

$$\frac{dy}{dx} = 0 \quad ; \quad r \leq 1$$

$$\frac{dy}{dx} = - \frac{2(1 - \kappa)xy}{(1 + \kappa)(x^2 + y^2)^2 + (1 - \kappa)(y^2 - x^2)} \quad ; \quad r > 1$$

from which the arrival times are obtained by integrating along the streamlines

$$t - t_0 = \int_{x_0}^x \frac{\phi}{u_x(x', y)} dx' \quad (\text{A-8})$$

where ϕ is the porosity. These results were used to compute the streamlines and the arrival time contours of Fig. 10 in the text.

REFERENCES

- [1] L. W. Lake, *Enhanced Oil Recovery*, (Prentice Hall, Englewood Cliffs, NJ, 1989); L. W. Gelhar, *Stochastic Subsurface Hydrology*, (Prentice-Hall, Englewood Cliffs, NJ, 1993).
- [2] W. G. Yeh, *Water Resources Res.*, **22**(2), 95 (1986); N. Z. Sun, *Inverse Problems in Groundwater Modeling*, (Kluwer Academic Publishers, Netherlands, 1994); D. McLaughlin and L. R. Townley, *Water Resource Res.*, **32**(5), 1131 (1996).
- [3] C. S. Matthews and D. G. Russell, *Pressure Buildup and Flow Tests in Wells*, (SPE Monograph Vol. 1, Dallas, 1967); R. C. Earlougher, *Advances in Well Test Analysis*, (SPE Monograph Vol. 5, Dallas, 1977); R. N. Horne, *Modern Well Test Analysis*, (Petroway, Palo Alto, CA, 1995).
- [4] S. C. Jones, in Soc. Petrol. Eng. 67th Annual Meeting Proceedings, SPE paper 24757 (1992); S. Ganapathy, D. Wreath, G. Pope and K. Sepehrnoori, Soc. Petrol. Eng. Formation Evaluation, **9**, 273 (1993).
- [5] C. F. Harvey and S. M. Gorelick, *Water Resources Res.*, **31**(7), 1615 (1995); B. J. Wagner, *J. Hydrology*, **135**, 275 (1992); A. Datta-Gupta, S. Yoon, I. Barman and D. W. Vasco, *J. Petrol. Tech.*, **50** (12), 72, (1998).
- [6] D. C. Brock and F. M. Orr, in Soc. Petrol. Eng. 66th Annual Meeting Proceedings, SPE paper 22614 (1991).
- [7] E. M. Withjack, S. M. Graham, and C. T. Yang, Soc. Petrol. Eng. Formation Evaluation, **7**, 447 (1991).
- [8] D. E. Lumley and R. A. Behrens, Soc. Petrol. Eng. Reservoir Evaluation and Engineering, **1**, 528 (1998).
- [9] L. Zhan and Y. C. Yortsos, 10th European Symposium on Oil Recovery Proceedings, Brighton, UK (1999).
- [10] Z-M. Yang and Y. C. Yortsos, *Phys. Fluids*, **9**(2), 286 (1997).
- [11] J. A. Sethian, *Level Set Methods and Fast Marching Methods*, Cambridge University Press, New York (1999).
- [12] *Spline Toolbox User's Guide*, The Mathworks, Inc. (1999).
- [13] R. F. Voss, in *The Science of Fractal Images*, (Springer-Verlag, New York, 1988); J.

- Feder *Fractals*, (Plenum Press, New York, 1988).
- [14] T. A. Hewett, in *Reservoir Characterization 2*, (Society of Petroleum Engineers, Houston, TX, 1989).
- [15] C. V. Deutch and A. C. Journel, *GSLIB: Geostatistical Software Library and User's Guide*, (Oxford University Press, Oxford, UK, 1992).
- [16] A. Tarantola, *Inverse Problem Theory, Methods for Data Fitting and Model Parameter Estimation*, (Elsevier Science Publishers, Amsterdam, 1987).
- [17] A. N. Tikhonov and V. Y. Arsenin, *Solutions of Ill-posed Problems*, (Halsted Press, New York, 1977).
- [18] P. R. Ballin, A. G. Journel and K. Aziz, *J. Can. Petrol. Tech.*, **31**(4), 52 (1992).
- [19] P. Berest, N. Rakotomalala, J.P. Hulin and D. Salin, *Eur. Phys. J. A.P* **6**, 309 (1999).
- [20] R. Lenormand, *Transport in Porous Media*, **18**, 245 (1995).

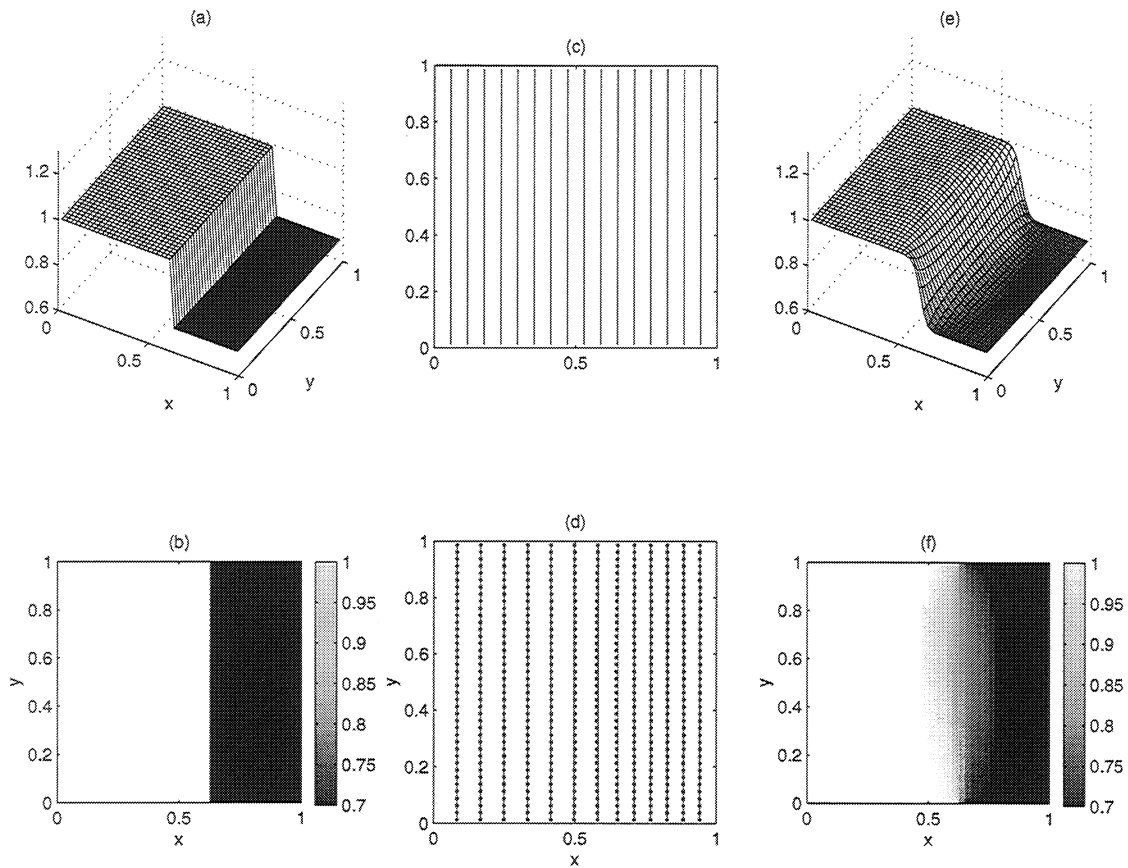


Figure 1: Application of the direct inverse method to a layered system shown in the left side: (a)-(b) actual permeability plots; (c) actual arrival times; (d) actual (solid lines) and inverted (dotted lines) potential profiles; (e)-(f) inverted permeability plots.

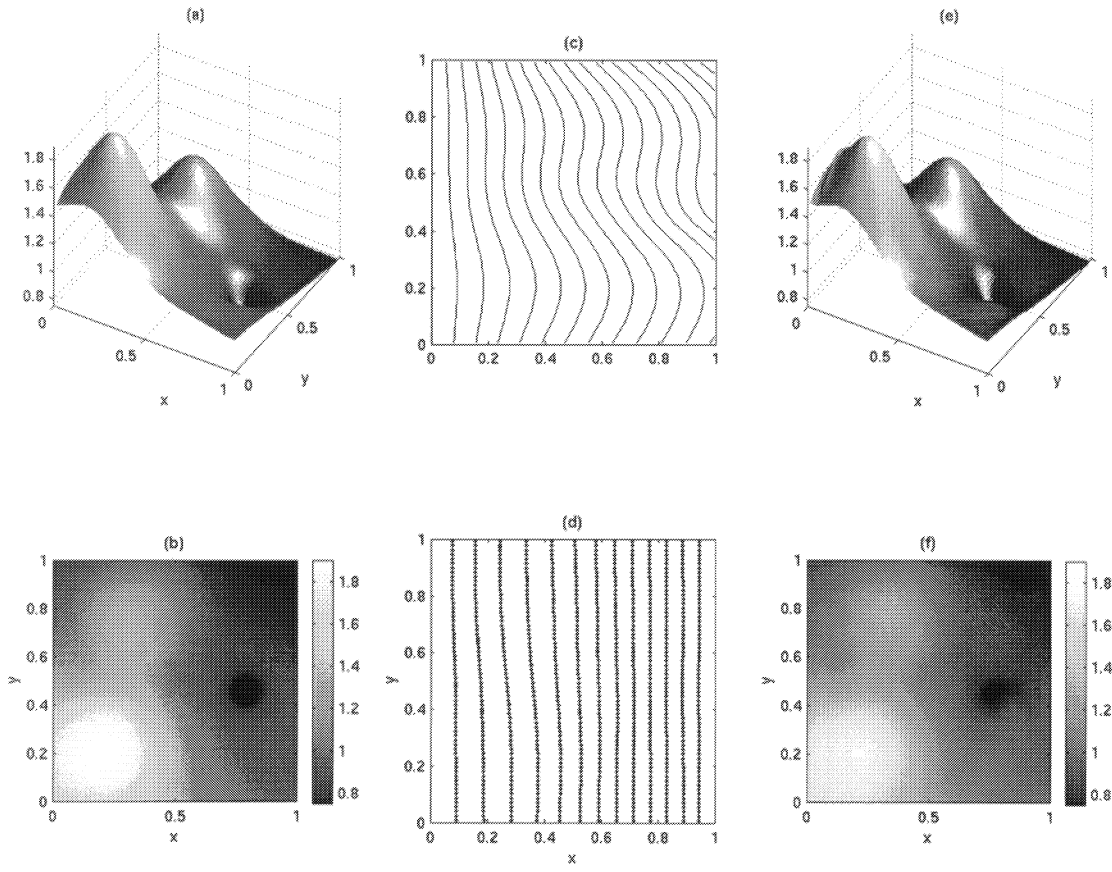


Figure 2: Application of the direct inverse method to a smoothly varying field shown in the left side: (a)-(b) actual permeability plots; (c) actual arrival times; (d) actual (solid lines) and inverted (dotted lines) potential profiles; (e)-(f) inverted permeability plots.

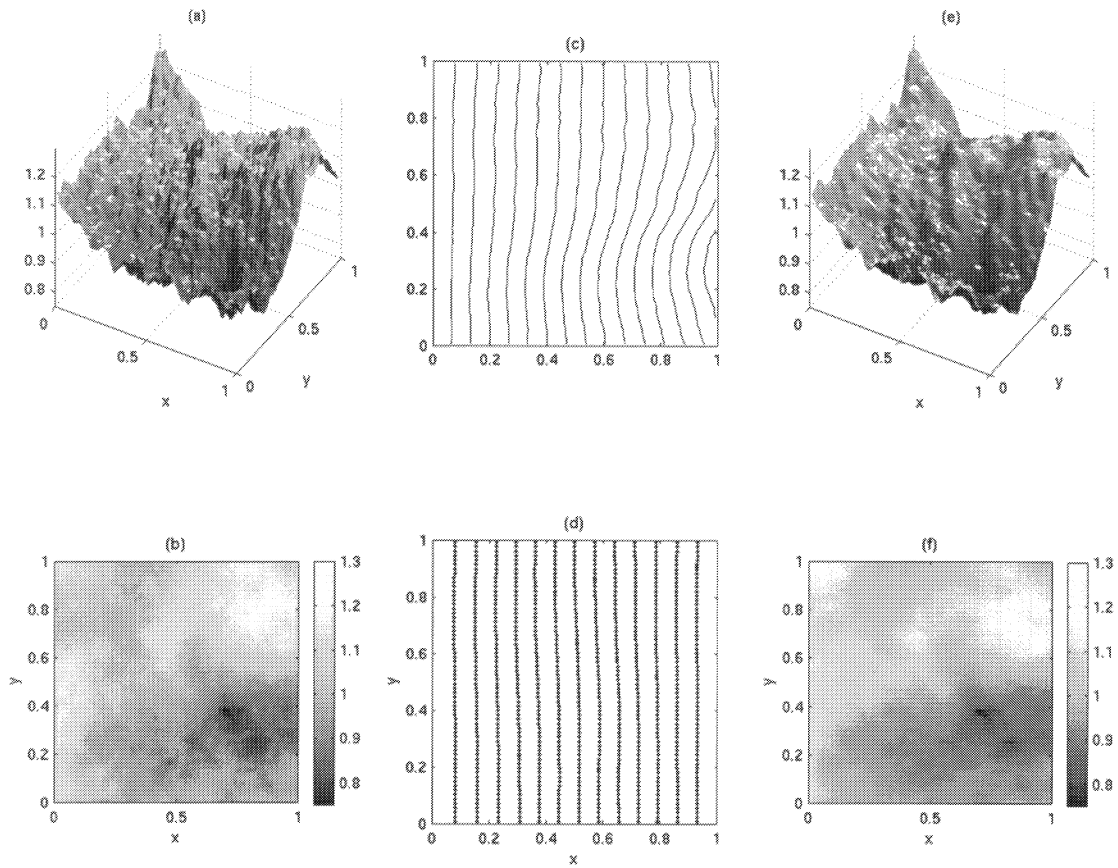


Figure 3: Application of the direct inverse method to an fBm field with $H = 0.8$ shown in the left side: (a)-(b) actual permeability plots; (c) actual arrival times; (d) actual (solid lines) and inverted (dotted lines) potential profiles; (e)-(f) inverted permeability plots.

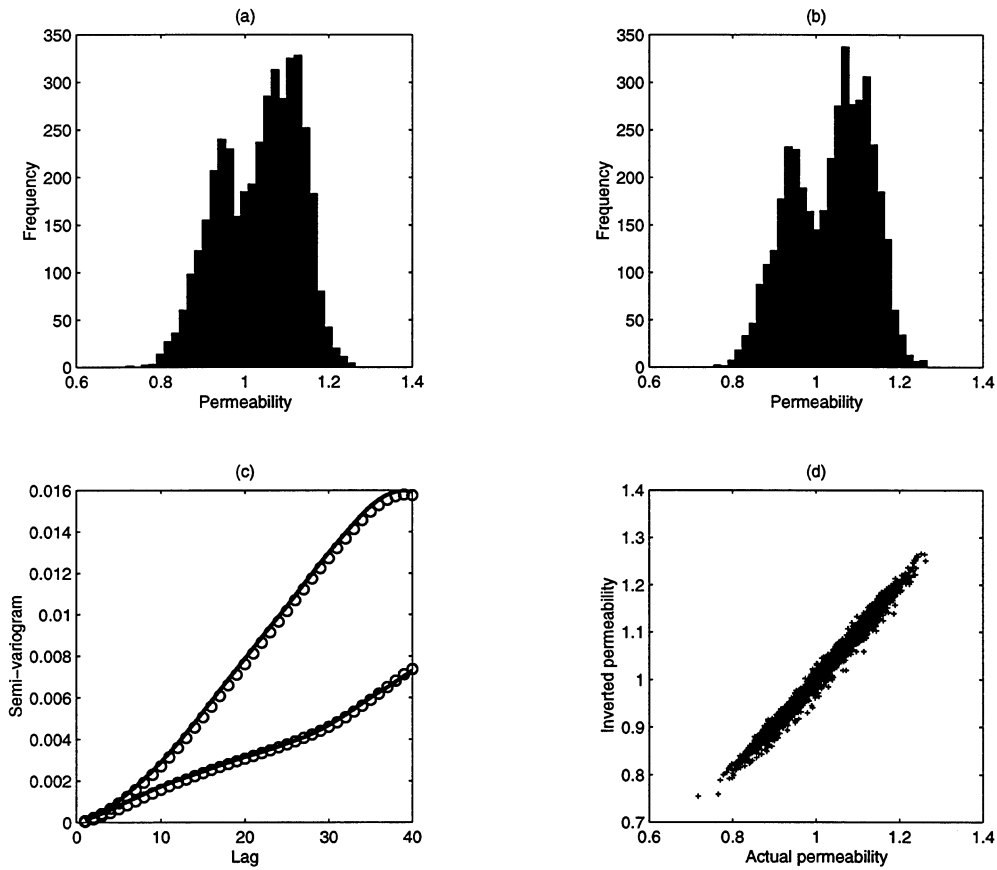


Figure 4: Statistical comparison between actual and inverted permeabilities of Fig. 3: (a) histogram of actual permeability; (b) histogram of inverted permeability; (c) semivariogram in two different directions of the actual (solid lines) and inverted (circles) data; (d) scatter plot of actual and inverted data.

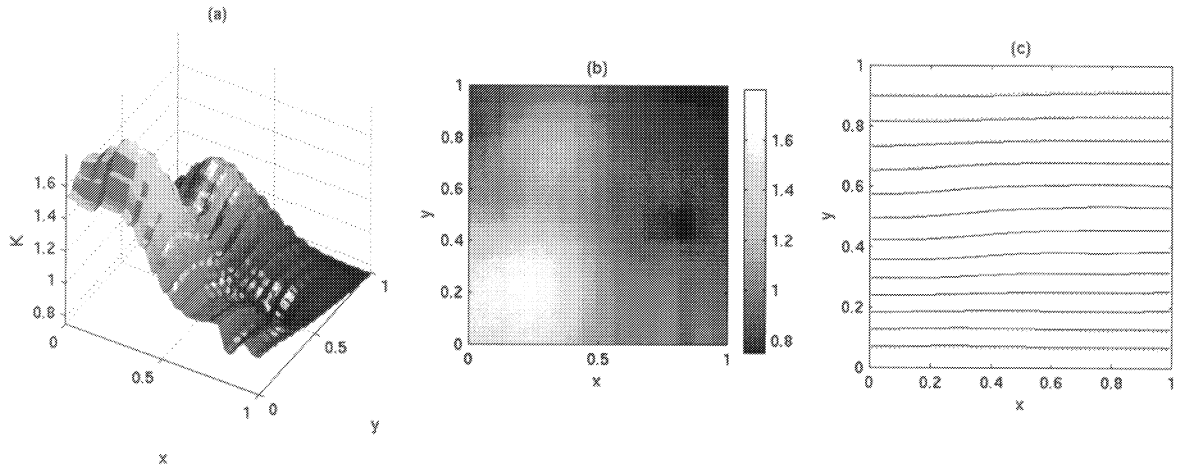


Figure 5: Application of the streamfunction approach to the medium of Fig. 2: (a)-(b) inverted permeability plots; (c) actual (solid lines) and inverted (dotted lines) streamlines.

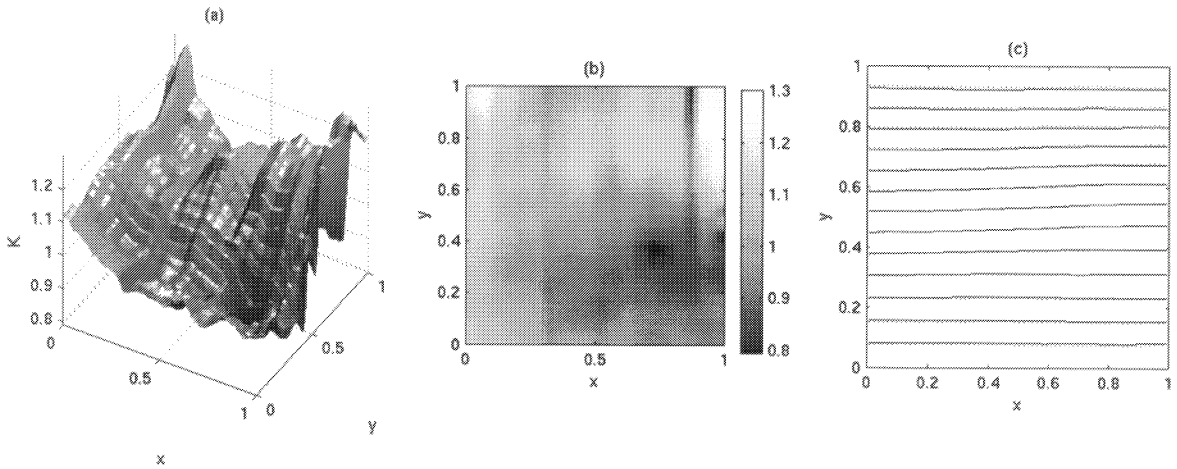


Figure 6: Application of the streamfunction approach to the medium of Fig. 3: (a)-(b) inverted permeability plots; (c) actual (solid lines) and inverted (dotted lines) streamlines.

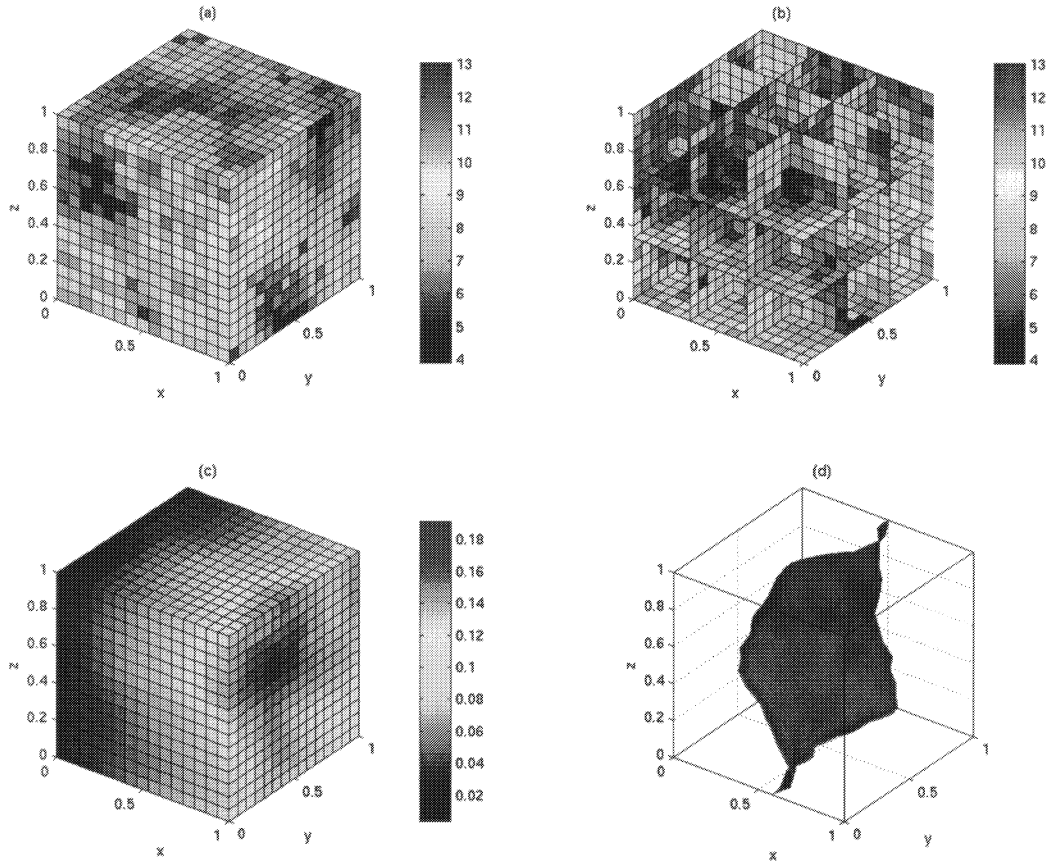


Figure 7: A 3-D permeability field and corresponding arrival times: (a)-(b) the actual permeability field in different cross-sections; (c) the arrival time distribution; (d) arrival time isosurface at $t = 0.07$.

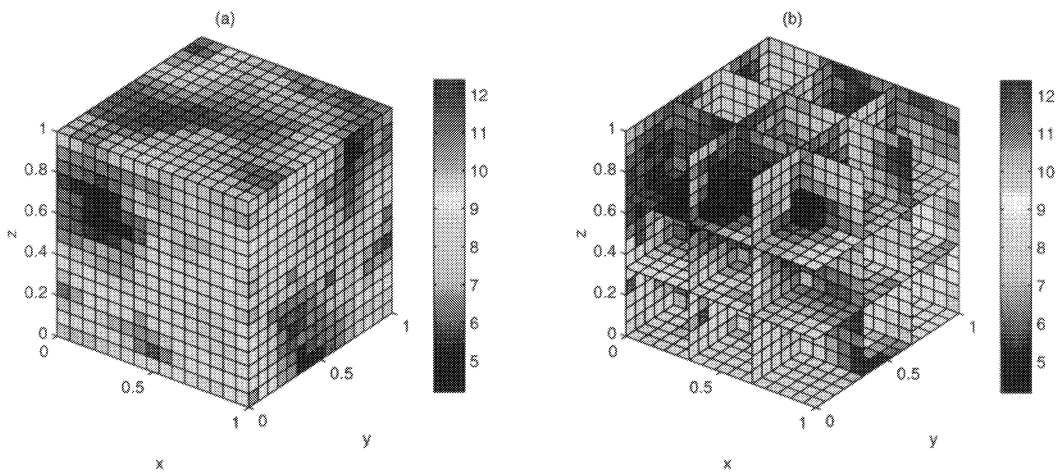


Figure 8: Application of the direct inverse method to the 3-D field of Fig. 7: (a)-(b) representation of the inverted data in different cross-sections.

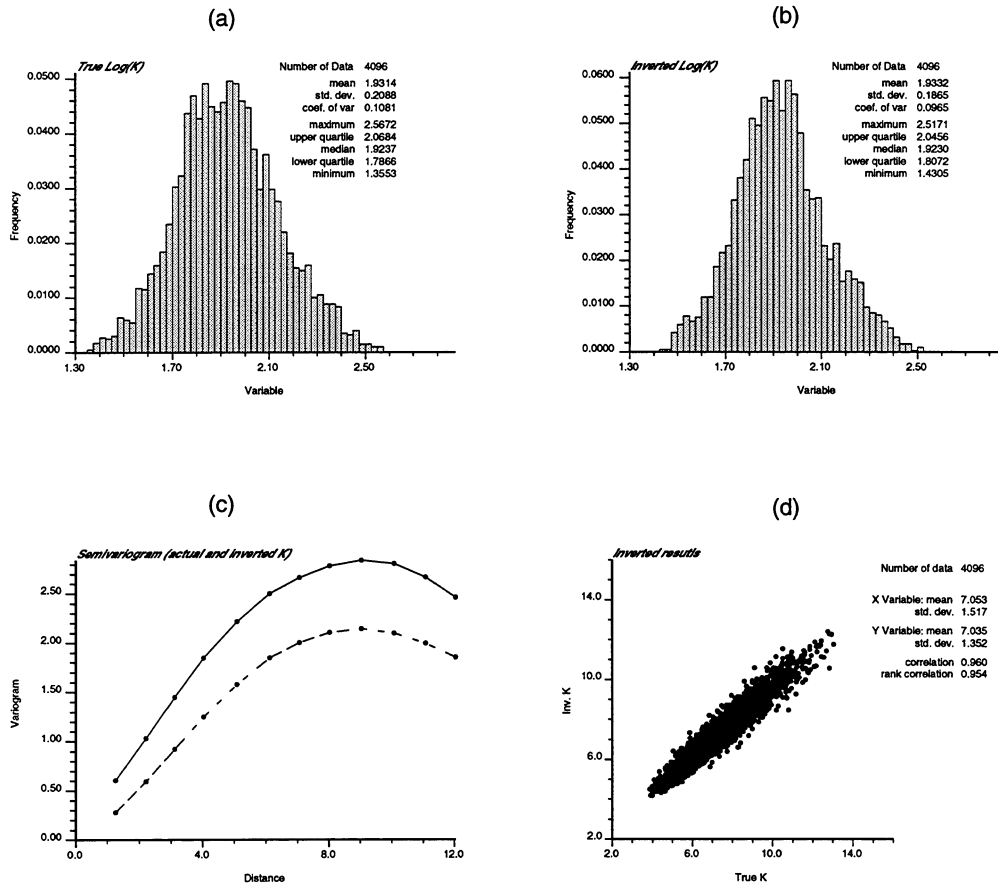


Figure 9: Statistical comparison between actual and inverted permeabilities of Fig. 8: (a) histogram of actual permeability; (b) histogram of inverted permeability; (c) omni-direction semivariogram of the actual (solid lines) and inverted (dash lines) data; (d) scatter plot of actual and inverted data.

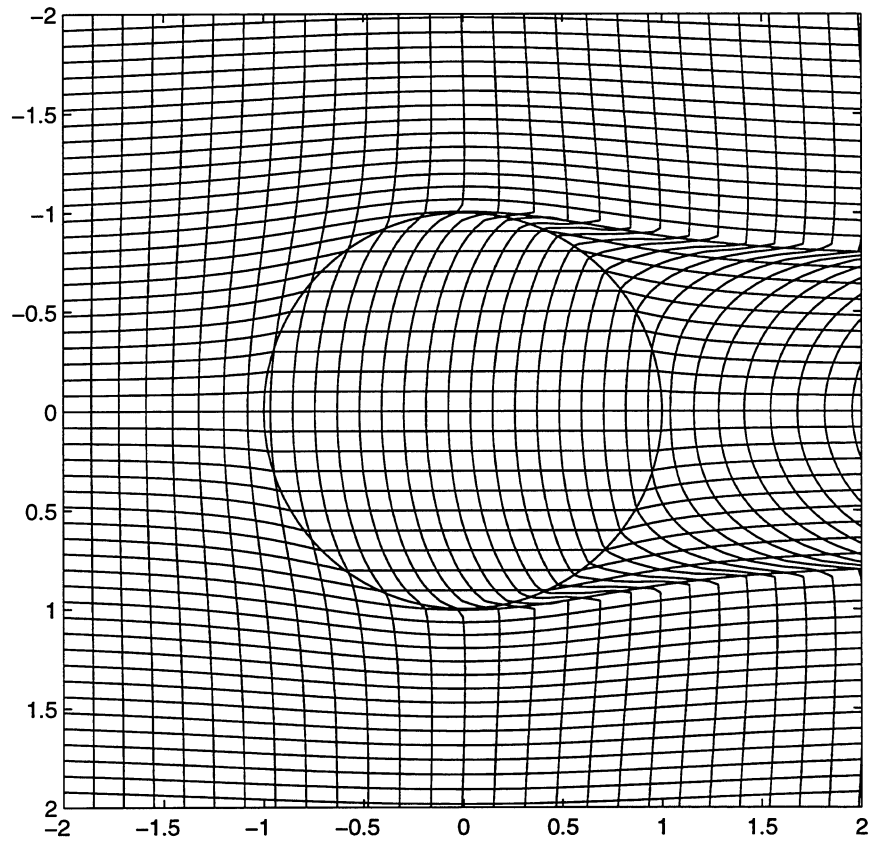


Figure 10: Streamlines and arrival time contours corresponding to a medium of uniform permeability in which a circular inclusion of lower permeability is embedded (permeability contrast is 0.6:1). The contours are calculated analytically (see Appendix). Displacement is from left to right.

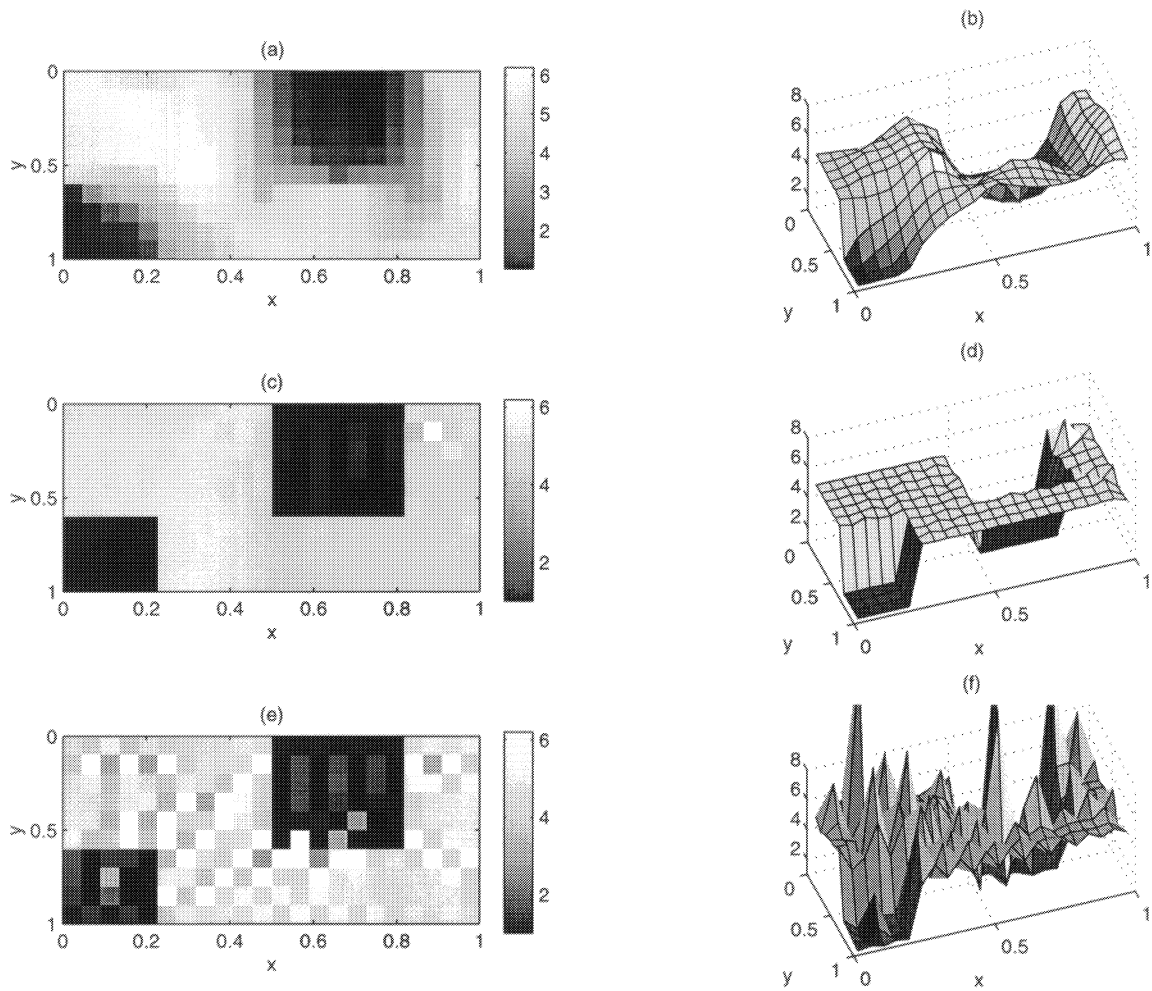


Figure 11: Application of the hybrid algorithm to a system with block discontinuities in permeability (permeability contrast is 1:5): Top two plots (a)-(b) show permeability estimates after steps 1-3 (Kriging). Middle two plots (c)-(d) show permeability estimates after step 4 (optimization). Note the closeness to the actual data. Bottom two plots (e)-(f) show permeability estimates using the optimization method but with a uniform permeability initial guess.

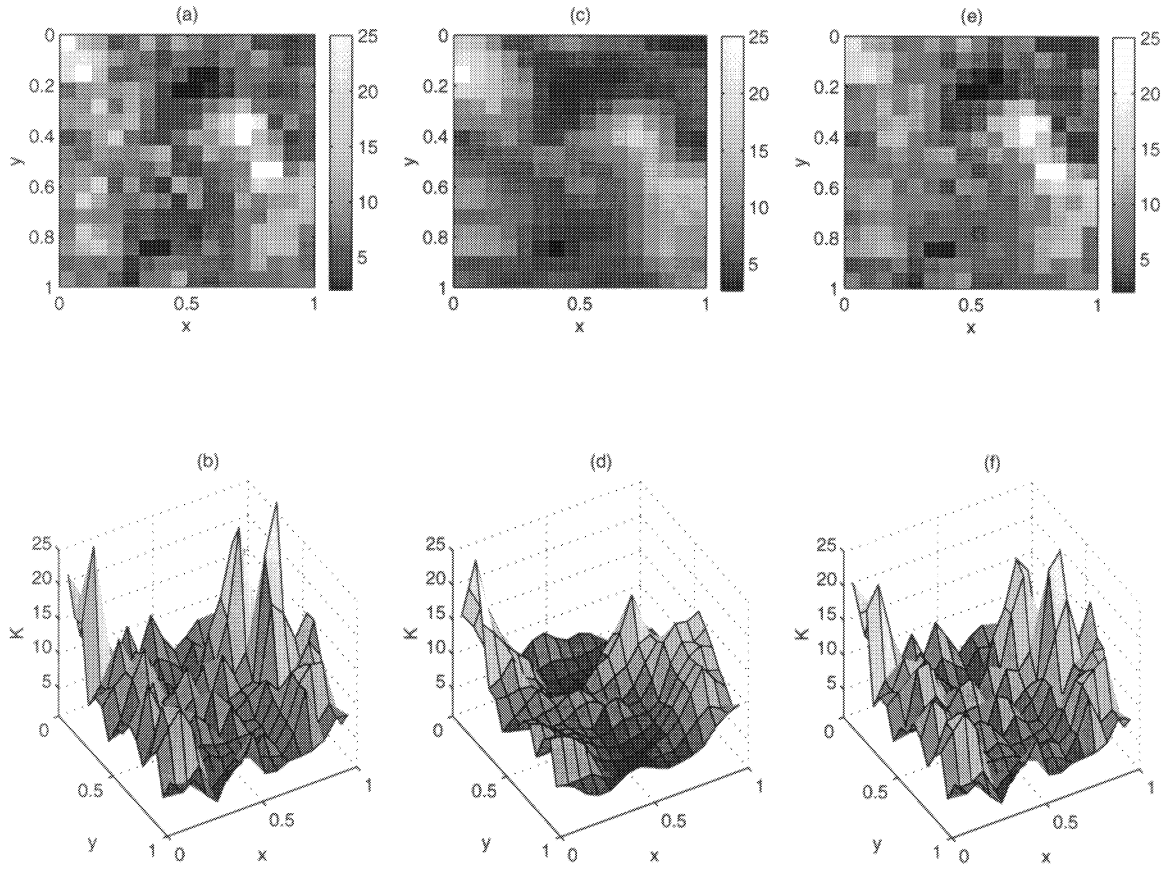


Figure 12: Application of the hybrid algorithm to a field with log-normal distribution with maximum contrast of about 10: (a)-(b) actual permeability plots; (c)-(d) plots of permeability estimates after steps 1-3 (Kriging); (e)-(f) plots of permeability estimates after step 4 (optimization). Note that the cut-off value of the colorbars in the image plots is set at 25.

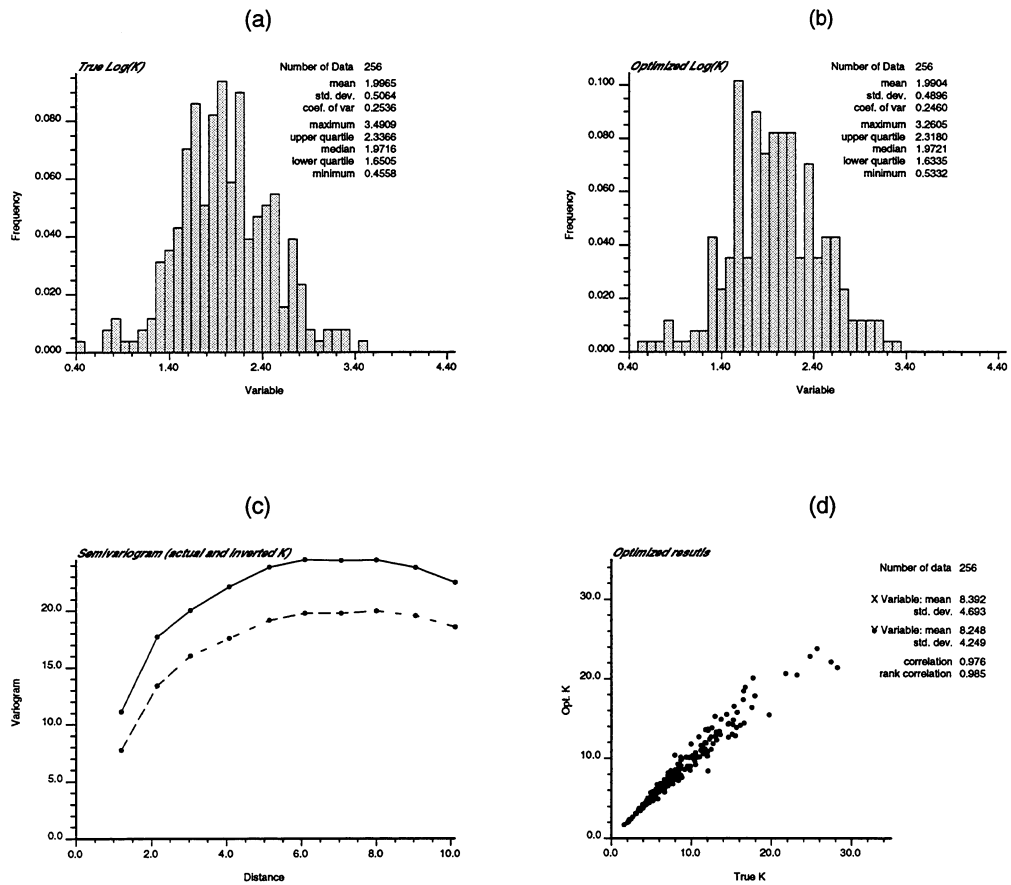


Figure 13: Statistical comparison between actual and inverted permeabilities of Fig. 12: (a) histogram of actual permeability; (b) histogram of inverted permeability; (c) omni-direction semivariogram of the actual (solid lines) and inverted (dash lines) data; (d) scatter plot of actual and inverted data.

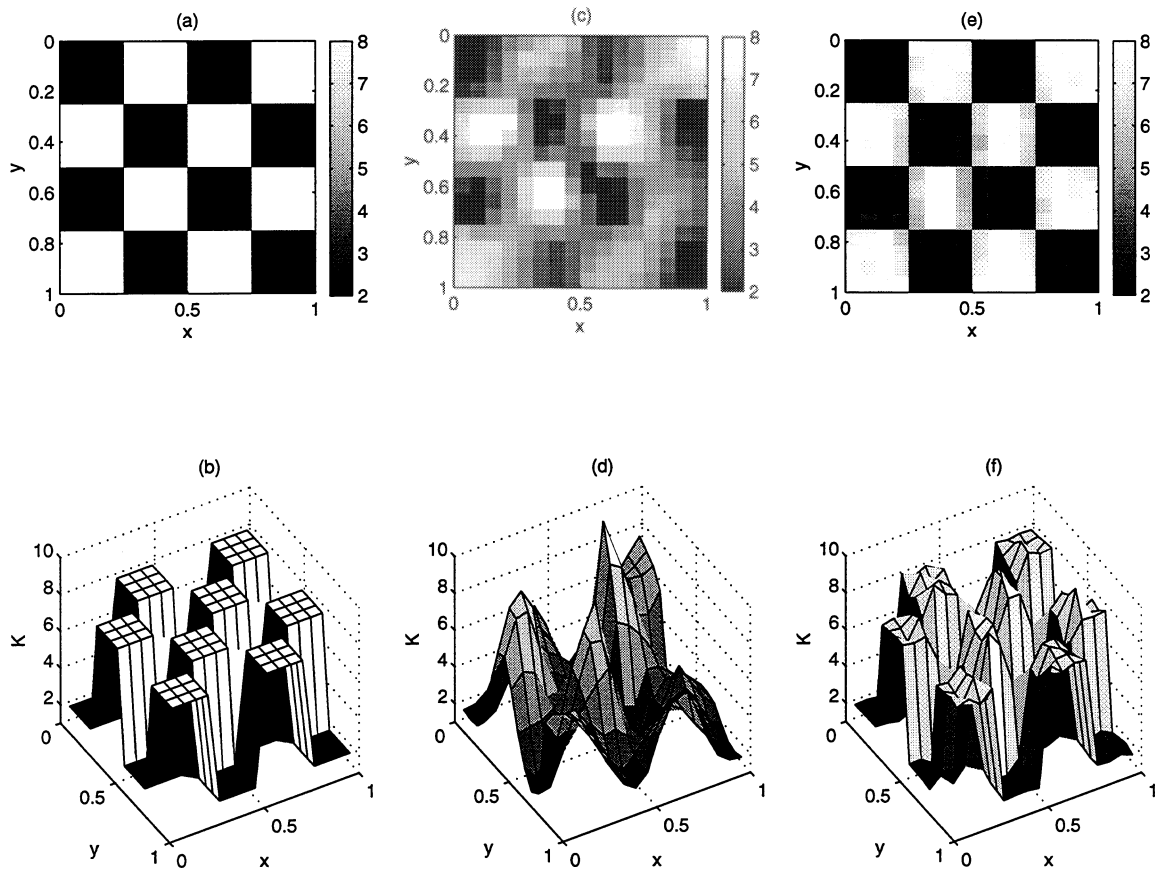


Figure 14: Application of the hybrid algorithm to a checkerboard permeability pattern (contrast is 2:8): (a)-(b) actual permeability plots; (c)-(d) plots of permeability estimates after steps 1-3 (Kriging); (e)-(f) plots of permeability estimates after step 4 (optimization). Note that the cut-off value of the colorbars in the image plots is set at 8.

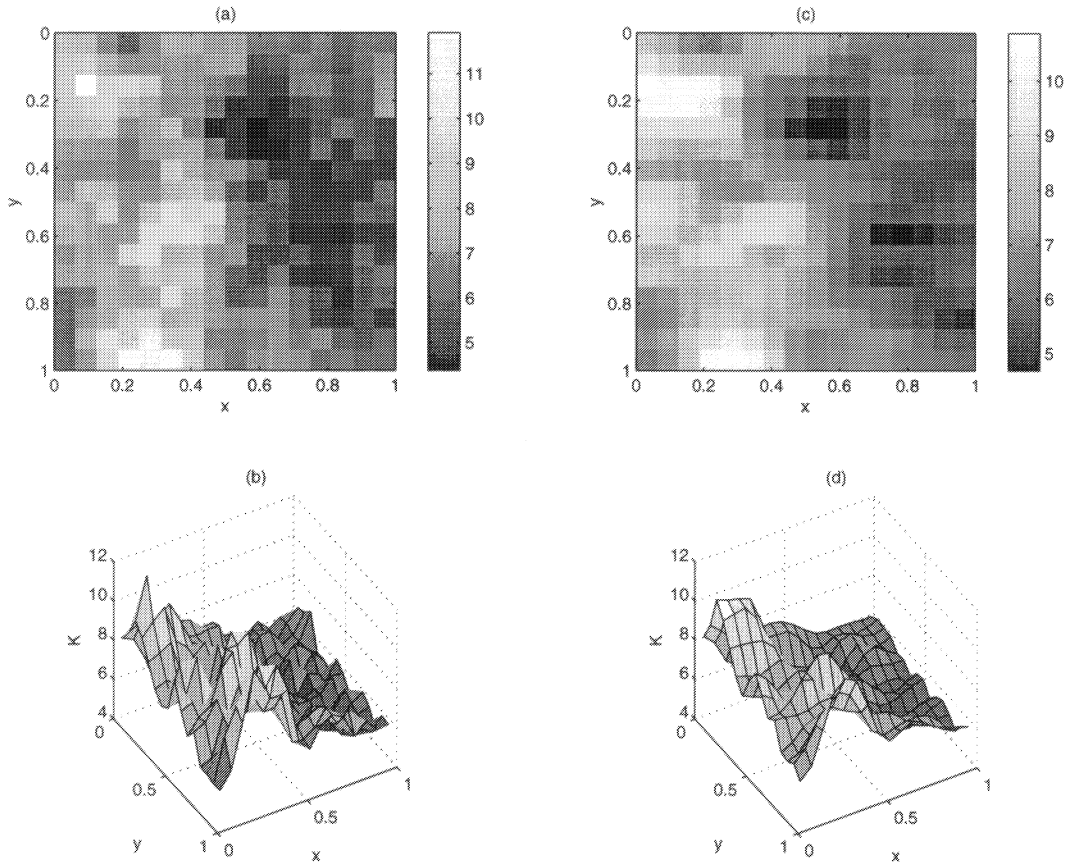


Figure 15: Application of the direct inverse method to an anisotropic field with known and fixed principal axes of anisotropy. Results for k_x : (a)-(b) plots of the actual permeability component values; (c)-(d) plots of the inverted permeability component values.

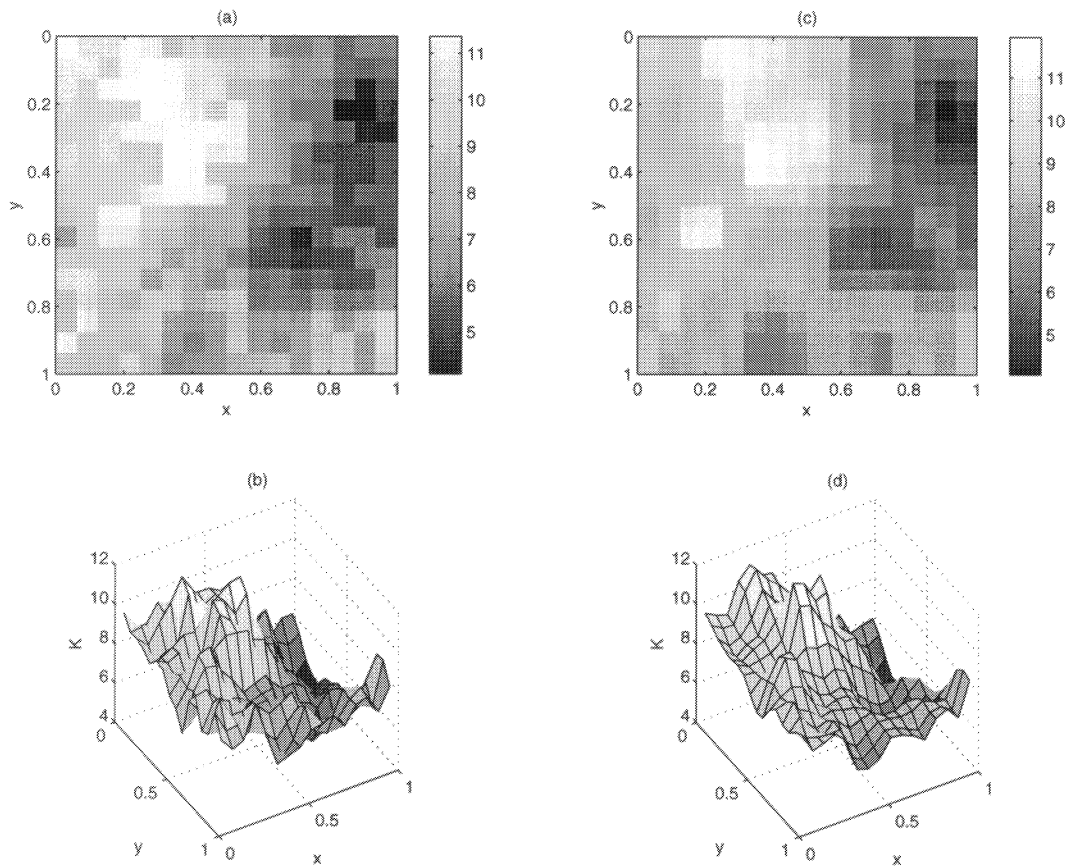


Figure 16: Application of the direct inverse method to an anisotropic field with known and fixed principal axes of anisotropy. Results for k_y : (a)-(b) plots of the actual permeability component values; (c)-(d) plots of the inverted permeability component values.

